nature portfolio

https://doi.org/10.1038/s41586-022-05002-7

Supplementary information

Imaging hydrodynamic electrons flowing without Landauer–Sharvin resistance

In the format provided by the authors and unedited

Supplementary materials for:

Imaging Hydrodynamic Electrons Flowing Without Landauer-Sharvin Resistance

Chandan Kumar, J. Birkbeck, J.A. Sulpizio, D. Perello, T. Taniguchi, K. Watanabe, O. Reuven, T. Scaffidi, Ady Stern, A.K. Geim and S. Ilani

Contents

S1. Device fabrication

Our devices consist of monolayer graphene encapsulated between two hexagonal boron nitride (hBN) layers, with a graphite flake underneath acting as a back-gate. These devices are assembled using the standard dry transfer technique[1]. Briefly, a polypropylene carbonate (PPC) coated polydimethylsiloxane (PDMS) was used to pick up the top hBN, monolayer graphene, and the bottom hBN, and this stack was then dropped on a graphite flake. After assembly, the heterostructure was annealed under ultra-high vacuum at 500 °C for ~ 8 hrs, followed by ironing with an AFM tip in contact mode. Both steps helped clean any residues from the surface of the top hBN and improve the sample's homogeneity by removing bubbles and ripples at the hBN-graphene interface[2]. Fig. S1a shows the optical image of the heterostructure. The monolayer graphene area (marked with a white dashed line) is free of bubbles/wrinkles. Next, we defined the Corbino disk using a standard electron beam lithography process, followed by reactive ion etching (RIE) with CHF_3 + O_2 and metal deposition of Cr (2 nm) / Au (80 nm) (Fig. S1b).

For making contact to the inner circular disk without electrically shorting to the outer metal ring, a bridge was defined on a small section of outer contact (highlighted by the dotted black line in Fig. S1c). The bridge was made by cross-linking polymethyl methacrylate (PMMA), using a high dose (x1000 regular dose) during electron beam lithography. Finally, in another electron beam lithography step, we defined a lead that passes over the cross-linked PMMA, ensuring that the inner circular disk and the outer contact ring are electrically isolated.

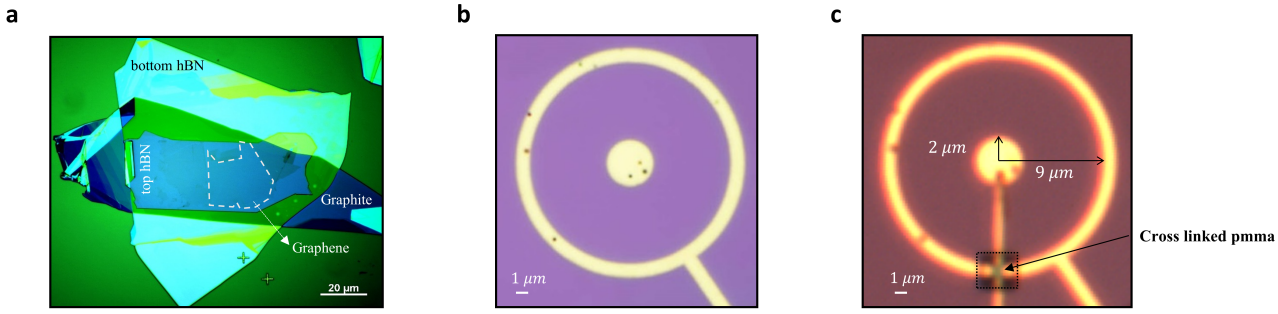

Fig. S1 | **Device fabrication**. **a.** Optical image of the heterostructure (hBN/Graphene/hBN/Graphite) after annealing and AFM ironing. The graphene region is demarcated with a white dashed line and is free of bubbles and wrinkles. The bottom graphite acts as a back-gate. The thicknesses of the top and bottom hBN are $40\ nm$ and $76\ nm$, respectively. **b.** Optical image of the heterostructure after making 1D contacts that define the Corbino disk geometry. **c.** Optical image of the Corbino disk after contacting the inner circular disk. The contact to the inner circular disk passes over cross-linked PMMA, defined over a small segment of outer contact (dashed black), electrically isolating the inner contact from the outer ring. The inner and outer radius of the graphene disk in this device are $r_{in} = 2\ \mu m$ and $r_{out} = 9\ \mu m$ (arrows), respectively.

S2. Transport measurements

We use standard lock-in techniques to measure the two-probe resistance between the inner and outer contacts of the Corbino disks as a function of carrier density, n, and temperature, T (from $6\ K$ to $140\ K$). We find that a significant component of the resistance comes from the lithographic lines that lead to the device. Using the Scanning SET imaging we accurately determine these line resistances by imaging the potential drop between the voltage source and the actual potential of the metal contact, measured by the SET. This line resistance was measured as a function of temperature and back-gate voltage, V_{BG} (which controls the carrier density) and found that it depends on T but not on V_{BG}. The measured total line resistance at $T = 6\ K$ is $R_{lines} = 515\ \Omega$ and it increases with increasing temperature, reaching $R_{lines} = 615\ \Omega$ at $T = 140\ K$. We subtract this SET-measured line resistance from the transport-measured two-probe resistance to obtain an effective four-probe resistance. Note that this four-probe resistance still includes the metal-graphene contact resistance, which includes both the fundamental Landauer-Sharvin component, and the component due to imperfect contacts. Fig. S2a plots this effective four-probe resistance as a function of carrier density, n, at various temperatures (see legend). Independently, we can determine the total device resistance directly from the SET measurements by reading out from the imaged $R(r)$ (e.g. Fig. 2b, main text) the difference in its value between the outer and inner contacts. The inset to Fig. S2a compares the SET measured device resistance (red dots) and the effective four-probe transport measured device resistance (blue) at $T = 6$ K. We can see an excellent agreement between the two measurements. (Note that the removed line resistance is independent of density and has excellent agreement over the entire density range). Plotting the conductance at $T = 6\ K$ as a function of $\sqrt{n}$ we can estimate the charge inhomogeneity in our samples from the flat region of conductivity near the Dirac point, which comes out to be $\delta n \sim 5 \times 10^9\ cm^{-2}$ (Fig. S2b). In the main text, data is presented for the electron-doped region. Most of the data (apart from Fig. 2d) are taken at a gate voltage of, $V_{BG} = 2\ V$ ($n = 4.5 \times 10^{11}\ cm^{-2}$), though we see similar phenomenology also at other densities (see e.g. section S7 below).

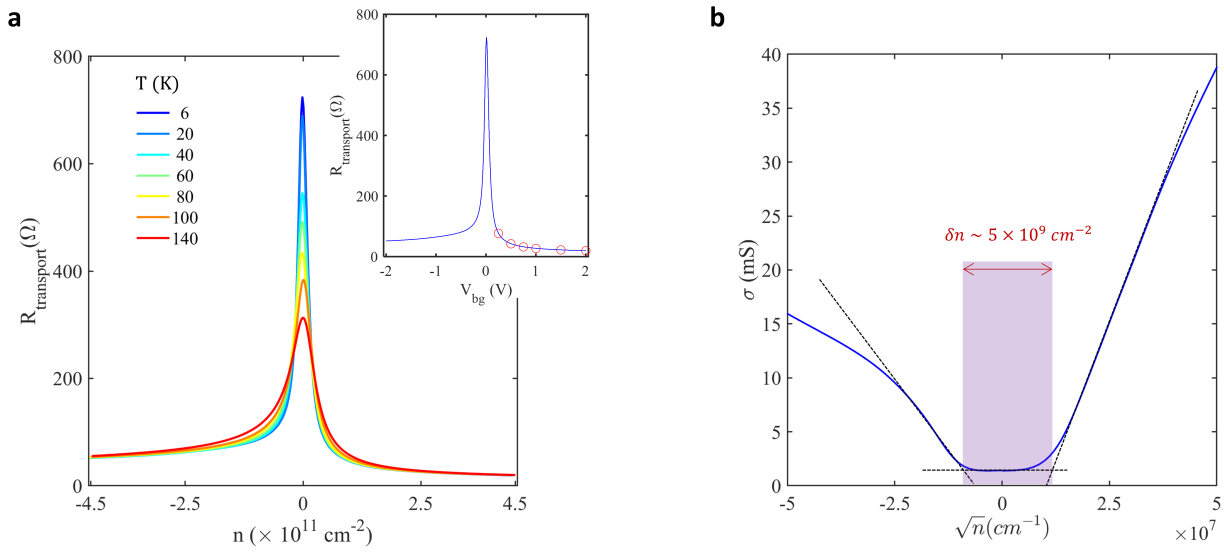

Fig. S2 | Transport measurements of the Corbino device in the main text. Main panel: effective four-probe transport resistance, $R_{transport}$, as a function of density, n, and at various temperatures, T (see legend). To obtain $R_{transport}$, we use standard lock-in measurements of the two-probe resistance between the Corbino disk's contacts. From this we subtract the lines resistance imaged using the scanning SET. We find that the line resistance depends on temperature but not on the back-gate voltage, V_{BG}. Inset: Corbino device resistance as a function of V_{BG} at $T = 6$ K. The blue line was taken from the main panel (transport measurement with line resistance subtracted) the red dots are obtained from imaging measurements of $R(r)$ using the scanning SET (e.g. Fig. 2b, main text). **b**. Transport measured conductivity, σ, at $T = 6$ K, plotted as a function of $\sqrt{n}$. The width of the plateau at the center provides an estimate for the charge disorder in the sample: $\delta n \sim 5 \times 10^9\ cm^{-2}$.

S3. Angular symmetry of the measured flow

In Figs. 2,3,4 of the main text we plot the resistance profile, $R(r)$, obtained by angular averaging of two-dimensional SET images of $R(x, y)$. This procedure is valid as long as the physics has a high degree of angular symmetry. We demonstrate this symmetry below using a specific measurement and note that a similar level of symmetry exists also for the data measured at other carrier densities and temperatures.

Figs. S3 plots a spatial scan of $R\ (x, y)$ measured at $B = 30\ mT, V_{BG} = 2\ V$ and $T = 100\ K$. Similar to the scan in Fig. 2a in the main text, which was performed at a different temperature and magnetic field, also here we see that the measurement exhibits excellent angular symmetry. Panels a and b show the same spatial scan, but with different averaging regions marked by a shaded "pizza" slice (outlined in black and red, respectively, in the two panels). The two resulting $R(r)$ profiles are shown in panel c with the corresponding colors. We can see that the two profiles are practically identical.

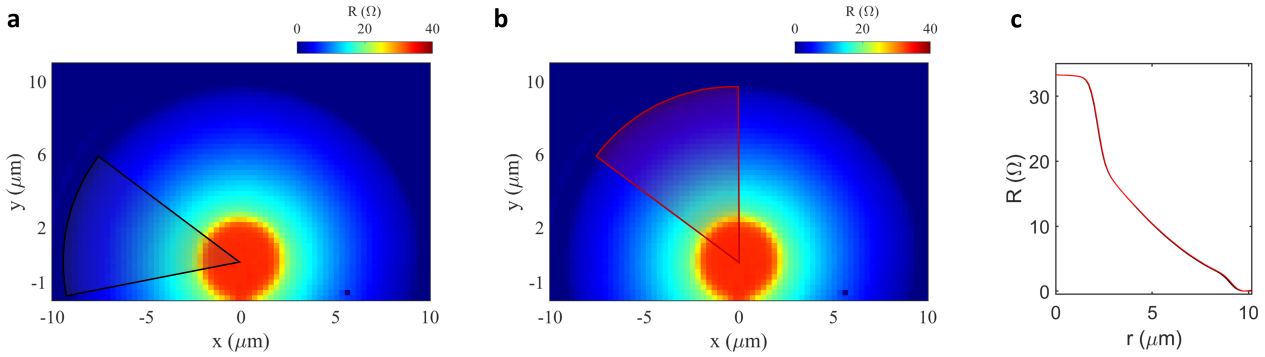

Fig. S3: **Angular symmetry of the measured data. a, b** In both panels we show the same spatial map of the resistance, $R(x,y)$, measured at $B = 30\ mT$, $V_{BG} = 2$ V and $T = 100$ K. The shaded slices with black (panel **a**) and red (panel **b**) outline marks the regions used for the angular averaging. **c.** The resistance profiles, $R(r)$, obtained from averaging over the slices in a and b, plotted with corresponding black and red colors.

S4. Measurement of the point spread function (PSF) of the imaging experiments.

The scanning SET measurements have a finite spatial resolution, determined by the scanning height of the SET above the graphene. This manifests in our scans as a spatial smearing with a point spread function (PSF) that depends on our scanning height. To accurately compare our measurements with the theory we extract the PSF from an independent imaging experiment and convolve the theory curves with this PSF. To determine the PSF we use an experiment that images the workfunction, $W(x,y)$, shown in Fig. S4a, and follow the recipe discussed in our previous work[3]. In contrast to the measurements of $R(x,y)$ which probe the potential that is generated by an electronic current (out of equilibrium), measurement of $W(x,y)$ probe the static (equilibrium) potential, in the absence of current. These are therefore measurements of completely independent properties.

In Fig. S4a we can see that the workfunction is constant throughout most of the graphene disk. On the central gold contact the workfunction is also constant, but with a different value. The transition between these two constants occurs very sharply, over lithographic scales. The workfunction image thus yields a sharp rise, ideal for determining the imaging PSF.

Fig. S4b plots the measured workfunction (blue dots) along the blue dashed radial line in Fig. S4a. Compared to an ideal step function positioned at $r_{in} = 2\ \mu m$ (black line), we see that the measurement is spatially smeared. The red curve shows the step function convolved with a PSF given by $g(r) = 1/\cosh^2\left(1.76\frac{r}{\sigma}\right)$. In our previous work[3] we demonstrated that this PSF describes well the smearing in

the experiment and that σ corresponds to our scanning height. We find a good fit between the measurement and the step function PSF-smeared with a height value of $\sigma = 0.85\ \mu m$. This is the PSF used in the main text.

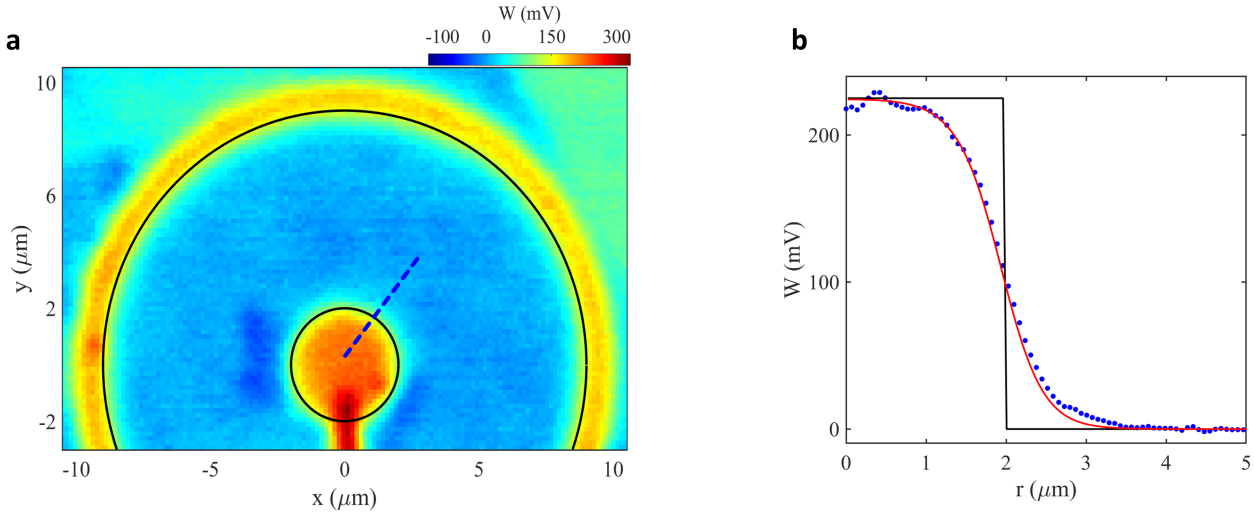

Fig. S4: **Obtaining the measurement's PSF from imaging of the workfunction. a.** Colormap of the measured workfunction, $W(x,y)$, over the Corbino disk. The solid black lines indicate the inner and outer radius of the graphene disk. **b.** Measured W (blue dots) along the dashed blue line in panel a. The black line shows a step function at the radius of the inner contact. The red line shows this profile smeared with the PSF $g(r) = 1/\cosh^2\left(1.76\frac{r}{\sigma}\right)$, where $\sigma = 0.85\ \mu m$. The smeared step function agrees well with the measured data.

S5. Determining the contact transparency from the measured resistance profile

As discussed in the main text, the two-probe resistance of a Corbino disk in the ballistic regime and with perfectly transmitting contacts, (transmission coefficient $T = 1$), is equal to the Sharvin resistance that corresponds to the radius of its inner contact, $R_{sh}^{in} = \frac{\pi h}{4e^2 K_F (2\pi r_{in})}$. Fig. 2b of the main text presents the radial dependence of resistance, $R(r)$, in the ballistic regime ($T = 6\ K$). Our measurement showed that the overall resistance (equivalent to two probe transport) is $19.5\ \Omega$, somewhat larger than $R_{sh}^{in} \sim 13.67\ \Omega$ at this density. We showed that a small part of this difference appears in the bulk and is due to a finite mean free path ($l_{MR} = 40\ \mu m$) that leads to a small ohmic bulk resistance. However, most of this difference happens at the contacts. For example, from the fitting in Fig. 2c we found that inner contact resistance step height is $0.82R_{sh}^{in}$, larger than the $0.5R_{sh}^{in}$ expected for an ideal contact. We will focus here only on the inner contact, because at low temperatures the physics there is simpler than at the outer contact (see section SI15 below). This increased contact resistance reflects a contact transmission that is

smaller than one. Following Landauer, we know that a finite transmission leads to a resistance of $\frac{1-T}{T}R_{sh}^{in}$. Adding this to the half Sharvin resistance expected for an ideal contact, we get:

$$R_{contact} = \frac{R_{sh}^{in}}{2} + \frac{1-T}{T}R_{sh}^{in} = R_{sh}^{in}\frac{(2-T)}{2T} \quad \text{(S5.1)}$$

Rearranging the above expression, we get:

$$T = \frac{2}{2R_{contact}/R_{sh}^{in}+1} \quad \text{(S5.2)}$$

Fig. S5 plots the contact transparency of the inner contact at $T = 6\,K$ as a function of carrier density, obtained by using equation S5.2 and $R_{contact}$ deduced from similar fits as in Fig. 2c, but for the resistance profiles measured at the different densities. We see that over the entire carrier density range the contact transparency is high, on par with the best transparencies achieved with graphene contacts[1,4].

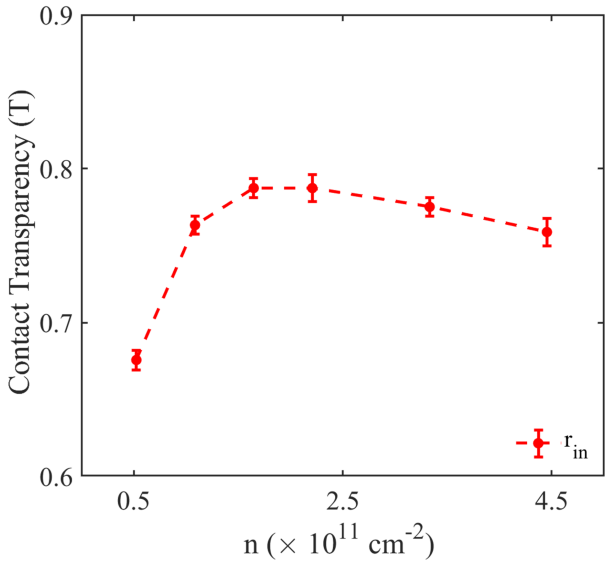

Fig. S5: **Density dependence of the inner contact transparency**. We fit $R(r)$ measured at $T = 6\,K$ and different carrier densities and obtain the height of the resistive step at the inner contact (see main text). Using equation S5.2 we obtain the corresponding contact transparency, presented in the figure as a function of the carrier density.

S6. Determining the momentum relaxing mean free path over the full temperature range.

As explained in the main text, when the temperature is high enough such that the electron flow is hydrodynamic, we can determine the momentum relaxing mean free path, l_{MR}, directly from measurements at finite magnetic fields (Fig. 4 in the main text). At low temperature, we can also determine l_{MR} from fitting the imaged resistance profile to Landauer-Sharvin + ohmic dependence + contact resistance, $R_{LS}(r) + R_{ohm}(r) + R_c^{in}(r) + R_c^{out}(r)$ (see Fig. 2c and corresponding text). In this section we use the theoretical expression for the temperature dependence of electron-phonon scattering to interpolate between these measurements and obtain the full temperature dependence of l_{MR}. This l_{MR} vs. T curve is then used together with Eq. (1) in the main text to obtain the traces in Fig. 3b.

In general, the momentum relaxing mean free path in graphene is determined by the scattering by disorder and phonons. We will term the former 'impurity scattering', although one has to keep in mind that disorder is not dominated by few isolated impurities but rather by a smooth potential modulation with long spatial scale caused by a distribution of many impurities spaced from the graphene by an hBN spacer. The corresponding disorder and electron-phonon mean free paths are l_{imp} and l_{e-ph}. The total momentum relaxing mean free path is then given by the Matthiessen sum rule of these two processes:

$$l_{mr} = (l_{imp}^{-1} + l_{e-ph}^{-1})^{-1} \tag{6.1}$$

In high-mobility graphene samples, like the ones in the current paper, the l_{mr} at low temperatures can be few tens of μm long, and is determined primarily by the impurity scattering. At elevated temperatures electron-phonon scattering kicks in, and this leads to a dramatic decrease in the mean free paths. At low temperatures, electron-phonon scattering is weak and goes as $\sim T^4$. It starts increasing dramatically when the temperature exceeds the Bloch-Gruneisen temperature, where the phase space for phonon scattering stops being limited by energy-momentum conservation, and phonons can scatter electrons to any direction on the Fermi surface. This temperature dependence of the electron-phonon scattering has been observed in the past and explained very successfully using the following model for electron-phonon induced resistance [1,5]:

$$\rho_{e-ph}(n,T) = \frac{8D_A^2 k_F}{e^2 \rho_m v_s v_F^2} f_s\left(\frac{\theta_{BG}}{T}\right) \tag{S6.2}$$

where $k_F = \sqrt{\pi n}$ is the Fermi momentum, D_A is the acoustic deformation potential, ρ_m is the mass density of graphene, v_F is the Fermi velocity, v_s is the longitudinal acoustic phonon velocity and f_s is the

Bloch Gruneisen function, given by $f_s(z) = \int_0^1 \frac{zx^4\sqrt{1-x^2}\, e^{zx}}{(e^{zx}-1)^2}\, dx$. The resistivity is translated to the e-ph mean free path using the standard relation valid for graphene:

$$l_{e-ph} = \frac{1}{\rho_{e-ph}(n,T)}\left(\frac{h}{2e^2 k_F}\right) \quad \text{(S6.3)}$$

We obtain the density dependence of the impurity mean free path at $T = 6\ K$ directly from our measurements (inset to Fig. 2d in the main text). These measurements are reproduced in blue dots in Fig. S6a together with a polynomial interpolation (blue line). At this temperature, the contribution of electron-phonon scattering is negligible, and thus this curve represents $l_{imp}(n)$. We further assume that the temperature dependence comes entirely from the temperature dependence of the e-ph scattering. If we add to $l_{imp}(n)$ the $l_{e-ph}(n,T)$ from equations (S6.1) - (S6.3) and use the parameters given in Ref[5] ($D_A = 21\ eV$, $\rho_m = 7.6e-7\ Kgm^{-2}$, $v_F = 1\times10^6\ ms^{-1}$ and $v_s = 2\times10^4\ ms^{-1}$) we obtain the total l_{MR} at elevated temperatures, shown by the different colored traces in Fig. S6a.

The orange, red, and dark red dots in Fig. S6a correspond to the l_{mr} obtained from magneto-resistance measurements (as described in the main text) at a density of $n = 4.5\times10^{11}\ cm^{-2}$ at $T = 100$ K (orange dot), $T = 140$ K (red dot) and $T = 180$ K (dark red dot). We see that these measurements nicely fit the above expression. This can be also seen when we plot l_{MR} vs. temperature (Fig. S6b). The above expression (black line) fits well the three experimentally measured points. This suggest that we can use this expression for obtaining the l_{MR} at temperatures between our low and high temperatures data points.

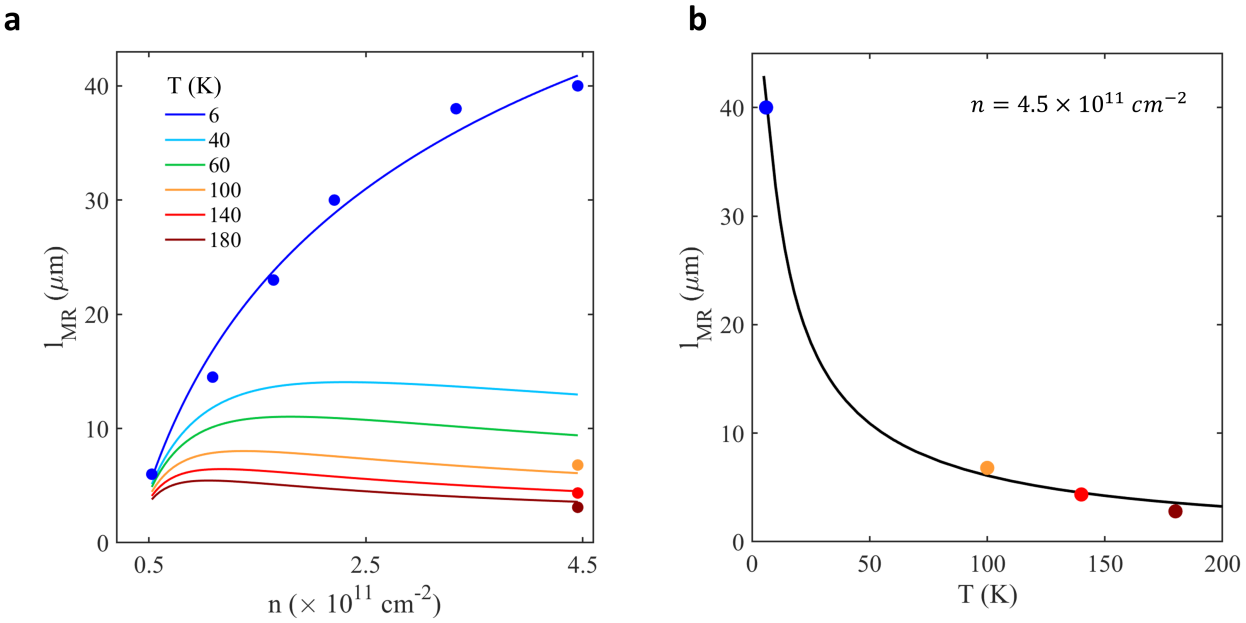

Fig. S6: l_{MR} vs. temperature and density. **a.** Measured mean free path as a function of carrier density at $T = 6$ K (blue dots), 100 K (orange dot), 140 K (red dot) and 180 K (dark red dot) (see text). The blue line is a polynomial fit through the data at 6 K. The lines corresponding to higher temperatures (see legend) include in addition the electron phonon scattering term (see text in this section). **b**. l_{MR} as a function of temperature at $n = 4.5 \times 10^{11} cm^{-2}$. The measured l_{MR} at $T = 6$ K (blue dot) 100 K (orange dot), 140 K (red dot) and 180 K (dark red dot) are in good agreement with the theoretical expression.

S7. Additional data at a different carrier density

In the main text, we present data at $V_{BG} = 2\ V$, corresponding to $n = 4.5 \times 10^{11}\ cm^{-2}$. Here, we present additional data from another carrier density ($V_{BG} = 1.5\ V,\ n = 3.3 \times 10^{11}\ cm^{-2}$), demonstrating similar behavior to that presented in the main text.

Fig. S7a shows the imaged $R(r)$ at $T = 6$ K and $n = 3.3 \times 10^{11}\ cm^{-2}$. This curve has similar characteristics as that in Fig. 2b. In Fig. S7b we use a similar fit as in the main text. The dashed line shows a fit to $R_{LS}(r) + R_c^{in}(r) + R_c^{out}(r)$, demonstrating that the measured bulk resistance is predominantly given by the Landauer-Sharvin resistance. Adding the ohmic term $R_{ohm}(r) = R_{sh}^{in}\frac{2r_{in}}{\pi l_{MR}}\log\left(\frac{r_{in}}{r}\right)$ with $l_{mr} = 38\ \mu m$ we obtain the excellent fit shown the dashed red curve.

Fig. S7c shows the bulk resistance $R_{bulk}(r) = R(r) - \left(R_c^{in}(r) + R_c^{out}(r)\right)$, as a function of temperature. We see similar trend to the measurements in the main text: the total bulk resistance first decreased with increasing temperature up to $T = 60$ K and then goes slightly up. Moreover, the spatial dependence within the bulk shows a similar evolution to the one shown in the main text: from a curved resistance profile at low temperatures (when plotted on a logarithmic r axis), $\sim$asin (r_{in}/r), to a linear profile, namely $\sim$log (r_{in}/r), at high temperatures.

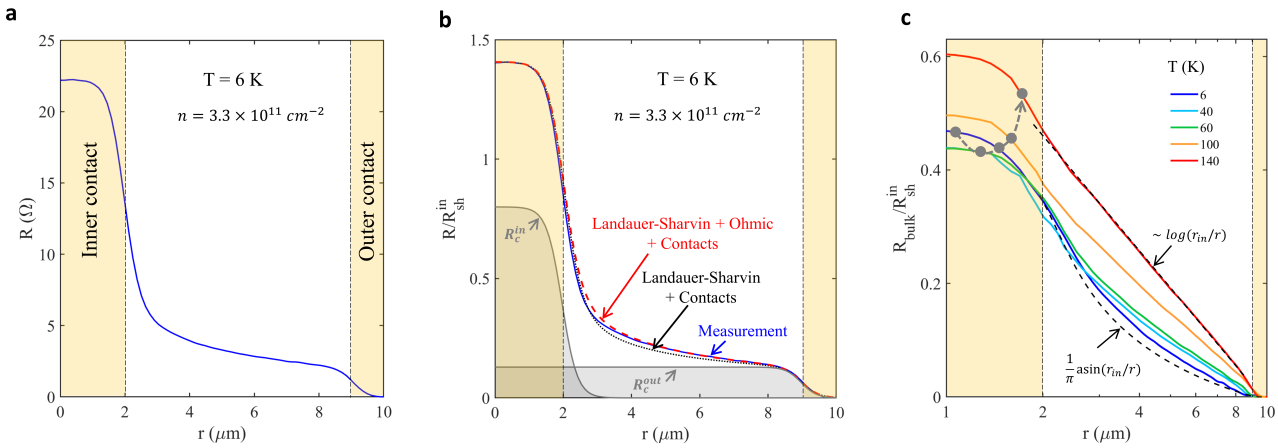

Fig. S7 | Measured resistance profiles at $n = 3.3 \times 10^{11}\ cm^{-2}$. **a**. Measured $R(r)$, at $T = 6\ K$. **b.** Breaking up the resistance to bulk and contact components. The PSF smeared contact resistances, $R_c^{in}(r)$ and $R_c^{out}(r)$ (grey), are as described in the main text. Dotted black line: Fit to $R_{LS}(r) + R_c^{in}(r) + R_c^{out}(r)$, where , $R_{LS}(r) = R_{sh}^{in}\frac{1}{\pi}\text{asin}\left(\frac{r_{in}}{r}\right)$ is the theoretically predicted Landauer-Sharvin bulk geometrical resistance. Red dashed line shows a fit to the same expression with the addition of $R_{ohm}(r) = R_{sh}^{in}\frac{2r_{in}}{\pi l_{MR}}\log\left(\frac{r_{in}}{r}\right)$, with $l_{MR} = 38\ \mu m$. **c.** Measured $R_{bulk}(r) = R(r) - \left(R_c^{in}(r) + R_c^{out}(r)\right)$ at various temperatures, T, normalized by R_{sh}^{in} and plotted with a logarithmic r axis.

S8. Imaging measurements on a second Corbino device

We performed measurements on a second Corbino disk with different dimensions, $r_{in} = 1\ \mu m$ and $r_{out} = 6\ \mu m$. The inset in Fig S8a shows the optical image of this device, fabricated using similar procedure as discussed in SI section 1.

Fig. S8a presents the measured $R(r)$ at $T = 6$ K and $n = 4.5 \times 10^{11}\ cm^{-2}$, where the transport is ballistic. This curve has the same characteristics to that in Fig. 2b. In Fig. S8b we use a similar fit as in the main text. The dashed line shows a fit to $R_{LS}(r) + R_c^{in}(r) + R_c^{out}(r)$, demonstrating that the measured bulk resistance is predominantly given by the Landauer-Sharvin resistance. Adding the ohmic term $R_{ohm}(r) = R_{sh}^{in} \frac{2r_{in}}{\pi l_{MR}} \log\left(\frac{r_{in}}{r}\right)$ with $l_{mr} = 27\ \mu m$ we obtain the excellent fit shown the dashed red curve.

Fig. S7c shows the bulk resistance $R_{bulk}(r) = R(r) - \left(R_c^{in}(r) + R_c^{out}(r)\right)$, as a function of temperature. We see similar trend to the measurements in the main text that: the resistance evolves from a curved resistance profile at low temperatures (when plotted on a logarithmic r axis), $\sim \text{asin}\,(r_{in}/r)$, to a linear profile, namely $\sim \log\,(r_{in}/r)$, at high temperatures.

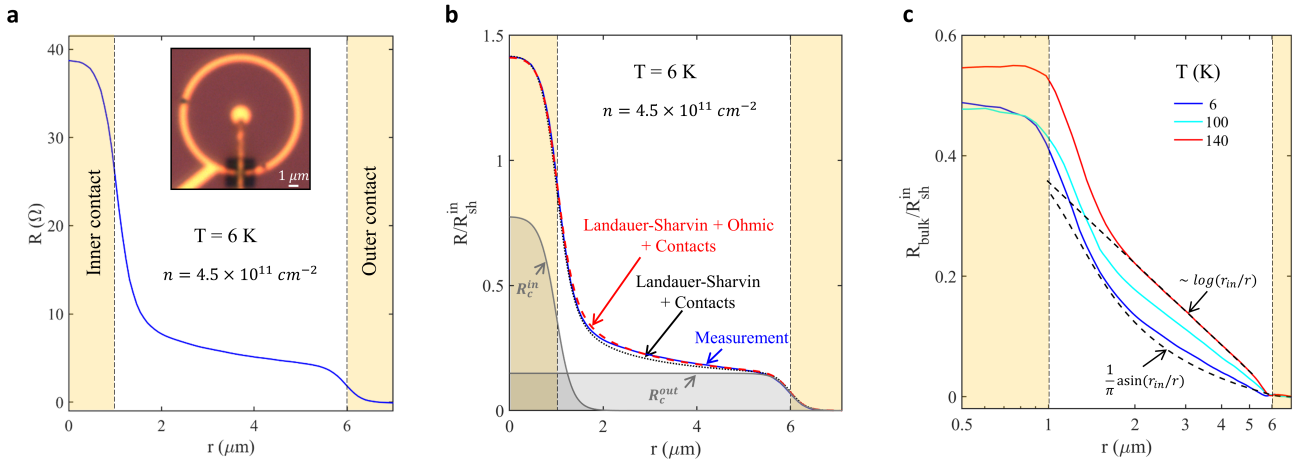

Fig. S8 | **Imaging of a second Corbino device**. **a**. Inset: optical image of the device. Main panel: measured $R(r)$, at $T = 6\ K$. **b.** Breaking up the resistance to bulk and contact components. The PSF smeared contact resistances, $R_c^{in}(r)$ and $R_c^{out}(r)$ (grey), are as described in the main text. Dotted black line: Fit to $R_{LS}(r) + R_c^{in}(r) + R_c^{out}(r)$, where , $R_{LS}(r) = R_{sh}^{in} \frac{1}{\pi} \text{asin}\left(\frac{r_{in}}{r}\right)$ is the theoretically predicted Landauer-Sharvin bulk geometrical resistance. Red dashed line shows a fit to the same expression with the addition of $R_{ohm}(r) = R_{sh}^{in} \frac{2r_{in}}{\pi l_{MR}} \log\left(\frac{r_{in}}{r}\right)$, with $l_{MR} = 27\ \mu m$. **c.** Measured $R_{bulk}(r) = R(r) - \left(R_c^{in}(r) + R_c^{out}(r)\right)$ at various temperatures, T, normalized by R_{sh}^{in} and plotted with a logarithmic r axis.

S9. Comparing resistance profiles at different temperatures but with similar l_{MR}.

An additional experimental check that gives a different way to assess the effect of electron hydrodynamics is to compare measurements performed at low and high temperatures, such that they have a similar momentum relaxing mean free path, l_{MR}. As explained earlier, at high temperatures, l_{MR} is determined primarily by electron-phonon scattering, so to obtain a similar l_{MR} at a low temperatures, the carrier density needs to be much closer to the charge neutrality point of graphene, such that disorder produces comparable scattering and therefore comparable l_{MR}. Figure S9 shows two resistance traces, $R(r)/R_{sh}$, measured at $T = 100\ K$, $n = 4.5 \times 10^{11}\ cm^{-2}$ (red) and $T = 6\ K$ and an order of magnitude smaller density $n = 5.25 \times 10^{10}\ cm^{-2}$ (blue). Both measurements have similar l_{MR} ($6.12\ \mu m$ in red curve and $6\ \mu m$ in blue curve, determined using the method outlined in section S6). Visibly, the resistance accumulated throughout the bulk in the $T = 100\ K$ measurement is significantly lower than the bulk resistance at $T = 6\ K$. The same difference is observed also after removal of the ohmic term using the additivity equation (Eq. 1 in the main text) and the above mentioned l_{MR} (Fig. S9b).

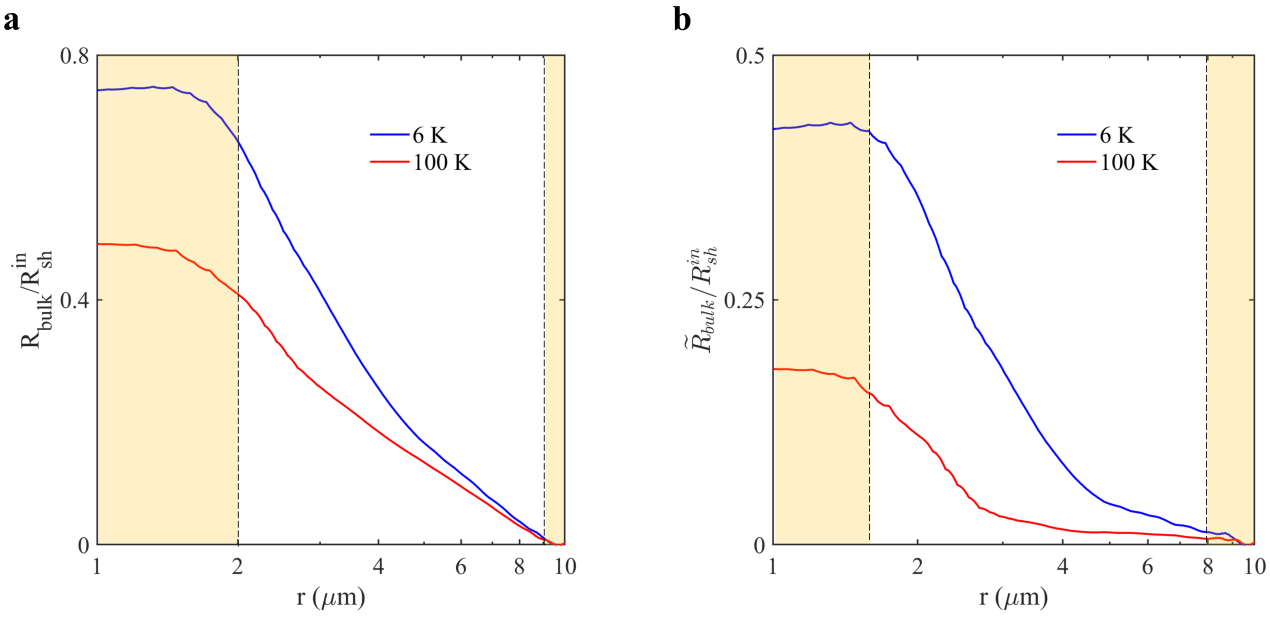

Fig. S9: Comparing resistance profiles at different temperatures but with the same l_{MR}. a. Comparison of resistance profiles, $R(r)/R_{sh}$, measured at elevated $T = 100\ K$ and $n = 4.5 \times 10^{11}\ cm^{-2}$ (red) and at $T = 6\ K$ and much closer to the charge neutrality point of graphene, $n = 5.25 \times 10^{10}\ cm^{-2}$. Both measurements have a similar l_{MR}: $6.12\ \mu m$ in the T = 100 K trace and $6\ \mu m$ in the $T = 6\ K$ trace, determined using the method outlined in section S6. **b**. Same as in panel a, but now after removal of the ohmic contribution due to momentum relaxing scattering using the additivity equation (Eq. 1 in the main text) and the measured values of l_{MR}.

S10. The Irrelevance of bulk magneto-resistance contributions.

In figure 4 in the main text, we presented measurements of the dependence of the resistance profiles on the magnetic field. These measurements showed that even small magnetic fields lead to significant increase in the overall device resistance. As explained in the main text, the quantity that is measured in a Corbino geometry is the inverse conductivity, σ_{xx}^{-1} rather than the longitudinal resistivity, ρ_{xx}. Whereas these two values are identical at $B = 0$, at a finite B the former has an additional term, originating from the Hall voltage, $\sigma_{xx}^{-1} = \rho_{xx}(1 + \rho_{xy}^2/\rho_{xx}^2)$. Since $\rho_{xy} \sim B$, and assuming that ρ_{xx} is independent of B (no bulk magnetoresistance), by measuring σ_{xx}^{-1} as a function of B we can determine ρ_{xy} and ρ_{xx} independently.

The main assumption taken in the analysis above is that ρ_{xx} is independent of B. To demonstrate its validity, we plot in Fig. S10 the magneto-resistance measured in the Corbino disk at $T = 140\ K$, $n = 4.5 \times 10^{11} cm^{-2}$ (taken from the inset of Fig. 4a,$r = 3\mu m$, and plotted here in red) and compare it with magneto-resistance measured in a Hall bar at $T = 150\ K$, $n = 5.5 \times 10^{11} cm^{-2}$ (blue), both normalized by their value at $B = 0$. The Hall bar experiment measures ρ_{XX} and thus allows us to determine the significance of bulk magneto resistance. We can clearly see that bulk magneto resistance measured in the Hall bar is negligible compared to the Hall voltage contributions measured in the Corbino disk. Specifically, we see that the coefficient of the B^2 term in the Corbino measurement is ~ 70 times larger than that in the Hall bar. This validates the main assumption used in analyzing the data in the main text.

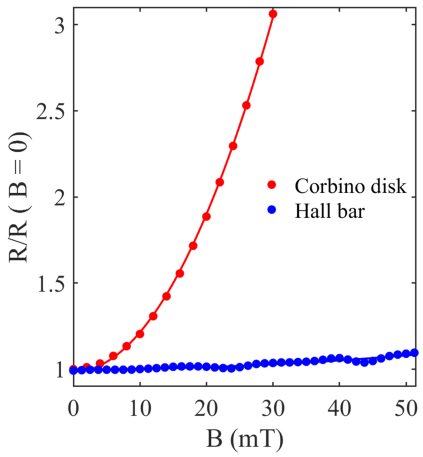

Fig. S10: Magnetoresistance in Corbino and Hall bar geometry: Red dots: measured $R(B, r = 3\mu m)$ in the Corbino disk at $T = 140\ K$ and $n = 4.5 \times 10^{11} cm^{-2}$ taken from the inset of Fig. 4a, and normalized by the value at $B = 0$. Red line: parabolic fit. Blue dots: Measured $\rho_{xx}(B)/\rho_{xx}(B = 0)$ in a Hall bar geometry at $T = 150\ K$ and $n = 5.5 \times 10^{11} cm^{-2}$. Blue line: parabolic fit.

S11. Measurement of the Hall angle profile at $T = 180\ K$

Figure S11 below presents the Hall angle profile measured at $T = 180\ K$. Similar to the data at $T = 140\ K$, presented in figure 4 of the main text, also here we measured the $R(r)$ profiles at several magnetic fields between $B = 0$ and $B = 30\ mT$ and determine the local Hall angle (blue dots Fig. S11) using the same procedure as outlined in the main text. As was observed at $T = 140\ K$, also here we see that the Hall angle is largest at the center of the Corbino channel and decays toward the contacts. Near the inner contact (three point after $r = 2\mu m$) we see a slight increase of $\tan(\theta_H)$ beyond the smooth curve. We believe that this is not physical, but reflects technical difficulties of the SET measurements very close to the contacts at this high temperature. Comparing the overall shape of the measured $\tan(\theta_H)$ to that measured at $T = 140\ K$, we can see that at $T = 180\ K$ the length scale of the decay of $\tan(\theta_H)$ is shorter than that observed at $T = 140\ K$. Thus, whereas at $T = 140\ K$ this decay propagated all the way to the center of the channel, and made the profile look more 'parabolic-like', here, we see a much clearer plateauing of $\tan(\theta_H)$ in the center of the channel. This is consistent with the dependence of the Gurzhi length on temperature. Moreover, this makes the determination of l_{MR} more independent of the possible values of l_{ee}. This is because at the channel center, $\tan(\theta_H)$ approaches its universal value, l_{MR}/R_c, which is independent of l_{ee}. A fit of the data using the theory in equation (2) in the main text gives $l_{MR} = 3 \pm 0.2\ \mu m$ and $l_{ee} = 0.6 \pm 0.2\ \mu m$. The colored curves in Fig S11 plot the theoretical profiles with the nominal value of l_{MR} ($3\ \mu m$) and various values of l_{ee}. We can see that the value at the center of the channel is indeed weakly dependent on l_{ee}, showing that our uncertainties in determining l_{MR} are quite small.

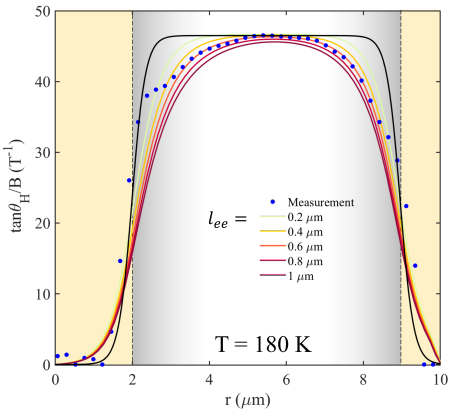

Fig. S11: Spatial dependence of the Hall angle, θ_H, at $T = 180\ K$**.** This graph is obtained from measured $R(r, B)$ for $B = 0 - 30\ mT$, and using the same procedure outlined in the main text (Fig. 4c). The figure plots $\tan(\theta_H)\ /B$ (since θ_H increases linearly with B) as a function of r (blue dots). The imaging resolution is apparent from the black curve, which is a boxcar function convolved with our imaging PSF. As predicted theoretically, $\tan(\theta_H)/B$ approaches a plateau at the center of the channel and drop gradually to zero near the contacts. The color traces show the results of the magneto-hydrodynamic theory (Eq. 2 in the main text) with $l_{MR} = 3\ \mu m$ and various values of l_{ee} (see key).

S12. The observed values of l_{ee}

Fig. S12 compiles the experimental values of l_{ee} deduced from representative published experiments together with those from the present work. These include values deduced from transport measurements in the vicinity geometry, values from transport in constriction geometry, values that we obtained in the experiments on the Poiseuille flow in a rectangular geometry, together with the values from the present work (see key). In the present work we have two independent ways of determining l_{ee}: the first is by comparing the Boltzmann simulations (Fig. 3c) with the value of the resistive step that we measure near the inner contact at $B = 0$ (Fig. 3b). The second is by fitting the magneto-hydrodynamically Hall angle profile (measured at finite B's) to the linearized Navier-Stokes theory (Eq. (2) in the main text). Both are plotted in the figure. Although there is considerable scatter in the experimental data, one can indeed see that the values determined here are generally larger by a factor of 1.5-2

In the figure we plot also the two theory lines taken from PRB 93,125410, which were used in the Supp. Info. of Nat. Phys. 13, 1182 to analyze the experiments on super-ballistic flow in constrictions. The first theory, denoted as $l_{ee}(T)$, is based on a microscopic RPA calculation of the quasiparticle lifetime. The second theory, denoted $l_{\nu}(T)$, is the calculated 'viscous' mean free path (we are using the terminology used in the above references). The two theories give similar trends, but also differ among themselves by a factor 2 to 3. The experimental data generally sits between these two theoretical estimates.

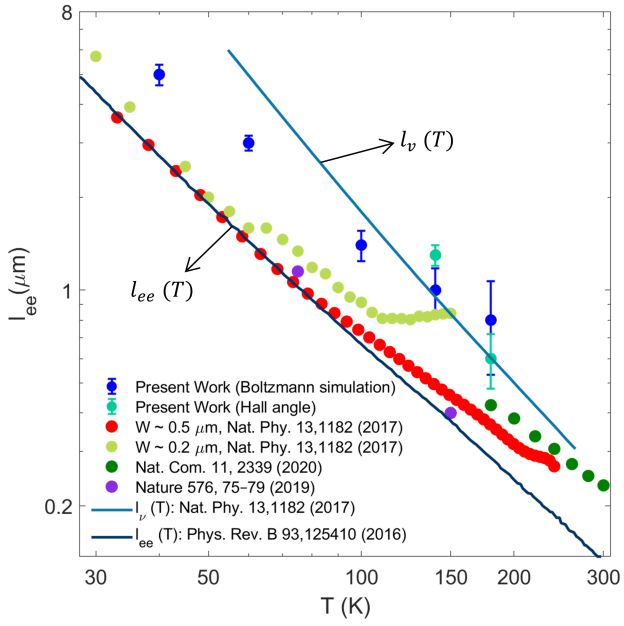

Fig. S12 Comparison of the obtained l_{ee} with published values. The figure compiles the values of l_{ee} vs. T from representative experiments as well the curves of different theories (see legend).

Several reasons can explain the differences between the measurements in the Corbino geometry and previous measurements in rectangular geometries. First, one should realize that the determination of l_{ee} from vicinity and constriction transport measurements was based mostly on fitting to Navier-Stokes and not Boltzmann equations. The former equations are strictly valid in the limit $l_{ee} \ll W$ (W is the relevant sample size), but this limit is not always obeyed in the experiments, especially at lower temperatures. For example, Fig. 3e in Nat. Phys. 13, 1182 plots the l_{ee} vs. T deduced from super-ballistic flow through a constriction whose width is $W = 0.5\ \mu m$, whereas below $T = 150\ K$ $l_{ee} > 0.5 \mu m$. This could introduce some numerical errors in the extracted l_{ee}. Second, measurements in rectangular channel and constriction geometries necessarily have physically-etched edges. The microscopic boundary conditions that these edges produce are not precisely known. The Navier-Stokes modeling often uses some free parameters to describe these boundary conditions, providing another source of uncertainty. We note however, that in the experiments imaging the Poiseuille flow profile (Nature 576, 75-75) there were less assumptions: the fit was done to Boltzmann equations, and the experimental data indicated that the etched boundaries can be described as fully diffusive to a good approximation (Extended Fig. 2). Yet, also there the obtained values of l_{ee} were shorter than in the present work. We should note though that in that paper it was also emphasized that at elevated temperatures the Boltzmann equations do not describe well the observed profiles (extended Fig. 9c), so clearly the existing theory is still incomplete.

In principle one might imagine that the Corbino results are less prone to assumptions, especially because they do not have physical edges. But we should note that there is also some uncertainty in the l_{ee} that we obtain in the present experiments. The first way we extract l_{ee} is by comparing the resistive step measured near the inner contact (Fig. 3b) with the Boltzmann simulations (Fig. 3c). But one should remember that in Fig. 3b we removed the contact resistance measured at the inner contact at T= 6 K and assumed that this contact resistance remains constant as a function of temperature. While this is a reasonable assumption, if the contact resistance does change with temperature (in the error bars we assumed 10% change) we could deduce a different value for l_{ee}. Note that this does not have any consequence on the main conclusions of the paper, which are based on the shape of the resistance profile in the bulk of the sample, especially the observation of perfect elimination of the Landauer-Sharvin bulk resistance. The second way that we extract l_{ee} is by fitting the magneto-resistance Hall profile to the Navier-Stokes theory (Eq (2)). In this way, there are some error bars on the values of the obtained l_{ee} as well, which are shown in Fig. S12.

S13. Derivation of Equation 1 in the main text

In this section we prove the identity:

$$R(r, L_{ee} = (l_{ee}^{-1} + l_{MR}^{-1})^{-1}, L_{MR} = \infty) = R(r, L_{ee} = lee, L_{MR} = l_{MR}) - \frac{\hbar}{2e^2 k_F l_{MR}} \log(r_{in}/r) \tag{S13.1}$$

which is equation (1) in the main text.$R(r, L_{ee}, L_{MR})$ is the bulk resistance profile with momentum-conserving and momentum-relaxing mean free paths of L_{ee} and L_{MR} correspondingly.

We make two general assumptions: 1) The existence of azimuthal symmetry, and 2) The use of the relaxation time approximation for momentum-relaxing and momentum-conserving scattering. Under these assumptions, the full Boltzmann equation reads as:

$$\vec{v}.\nabla\chi + (l_{ee}^{-1} + l_{MR}^{-1})(\chi - \bar{\chi}) - l_{ee}^{-1} 2\cos(\theta)\,\overline{\chi\cos(\theta)} = 0 \tag{S13.2}$$

where $\chi(r, \theta)$ is the Boltzmann function describing the distribution of the carrier's momenta direction, given by θ at location r, and $\bar{\chi}$ is its averaging over θ.

We rewrite equation (S13.2) as,

$$\vec{v}.\nabla\chi + (l_{ee}^{-1} + l_{MR}^{-1})(\chi - \bar{\chi}) - (l_{ee}^{-1} + l_{MR}^{-1}) 2\cos(\theta)\,\overline{\chi\cos(\theta)} + l_{MR}^{-1} 2\cos(\theta)\,\overline{\chi\cos(\theta)} = 0 \tag{S13.3}$$

or,

$$L_0\chi + l_{MR}^{-1} 2\cos(\theta)\,\overline{\chi\cos(\theta)} = 0 \tag{S13.4}$$

where L_0 is the Boltzmann equation for a modified problem with $L_{MR} = \infty$ and $L_{ee} = (l_{ee}^{-1} + l_{MR}^{-1})^{-1}$.

Denoting the solution of L_0as χ_0, we look for a solution of the form $\chi = \chi_0 + \delta\chi(r)$.

We find

$$L_0\delta\chi + l_{MR}^{-1} 2\cos(\phi\theta)\,\overline{\chi\cos(\theta)} = 0$$

$$\cos(\theta)\,\partial_r\delta\chi + l_{MR}^{-1} 2\cos(\theta)\,\overline{\chi\cos(\theta)} = 0$$

$$\partial_r\delta\chi + l_{MR}^{-1} j = 0 \tag{S13.5}$$

and thus

$$\delta\chi = -l_{MR}^{-1}\frac{I}{2\pi}\left(\log(r_{in}) - \log(r)\right) \tag{S13.6}$$

S14. Boltzmann simulations of interacting flow in a Corbino geometry

To model electron flow through the graphene channels, we employ an approach based on the Boltzmann equation[6–9] that incorporates the effects of both electron-impurity and electron-phonon scattering as well as electron-electron interactions:

$$\partial_t f + \vec{v} \cdot \nabla_{\vec{r}} f = \frac{\partial f}{\partial t}|_{scatt}, \tag{S14.1}$$

where the scattering integral,

$$\frac{\partial f(\vec{r},\vec{v})}{\partial t}|_{scatt} = -\frac{f(\vec{r},\vec{v}) - n(\vec{r})}{\tau} + \frac{2}{\tau_{ee}} \vec{v} \cdot \vec{j}(\vec{r}), \tag{S14.2}$$

has two contributions: one from momentum-relaxing scattering, with a rate $\frac{1}{\tau_{MR}}$, and one from momentum-conserving, electron-electron scattering, with a rate $\frac{1}{\tau_{ee}}$. This equation describes the evolution of the semiclassical occupation number $f(\vec{r},\vec{v})$ for a wave packet at position $\vec{r}$ and velocity $\vec{v}$, where $n(\vec{r}) = \langle f \rangle_{\vec{v}}$ is the local charge density, $\vec{j}(\vec{r}) = \langle f\vec{v} \rangle_{\vec{v}}$ the local current density, $\langle \dots \rangle_{\vec{v}}$ is the momentum average, and $\frac{1}{\tau} = \frac{1}{\tau_{MR}} + \frac{1}{\tau_{ee}}$. For the sake of simplicity, we consider the case of a circular Fermi surface with $\vec{v} = v_F \hat{\rho}(\theta)$, where $\hat{\rho}$ is the radial unit vector at angle θ. Mean free paths are then simply defined as $l_{MR(ee)} = v_F \cdot \tau_{MR(ee)}$. The term proportional to τ_{ee}^{-1} is the simplest momentum-conserving scattering term that can be written, assuming that the electrons relax to a Fermi-Dirac distribution shifted by the drift velocity[6,10–12].

The sample is a Corbino disk with inner radius r_{in} and outer radius r_{out}. We use polar coordinates in real space as well, with radius r and angle ϕ. Thanks to a rotational symmetry, the ϕ variable drops out of the calculation. Combining everything, the Boltzmann equation takes the form:

$$cos(\theta)\partial_r f - sin(\theta)\frac{1}{r}\partial_\theta f = -\frac{f(\mathrm{r},\theta) - n(\mathrm{r})}{l} + \frac{2}{l_{ee}} \vec{v} \cdot \vec{j}(\mathrm{r}) \tag{S14.3}$$

with $= v_F \tau$, $n(r) = \frac{1}{2\pi}\int d\theta\, f(r,\theta)$ and where $j_r(r) = \frac{1}{2\pi}\int d\theta\, f(r,\theta)\cos(\theta)$ is the radial current (the azimuthal current is zero by symmetry).

The rapid transition from a practically-infinite density of states in the metal contact, to the finite density of states at the graphene channel next to it, imposes the following boundary condition:

$$f(r = r_{min}, -\pi/2 \leq \theta \leq \pi/2) = f_{in}$$
$$f(r = r_{max}, \pi/2 \leq \theta \leq 3\pi/2) = 0, \quad \text{(S14.4)}$$

where f_{in} is a constant whose value is set to fix the total current.

The resulting integrodifferential equation is solved numerically using the method of characteristics[13] to invert the differential part of the equation, and an iterative method to solve the integral part.

Based on the solution for f, one finds the total current as $I = 2\pi j_r$ and the electrochemical potential as the electron density $n(r)$ divided by the density of states at the Fermi level.

Further, the contact resistance can be deduced by assuming the following form for f at the two contacts: $f(r = r_{min} - \varepsilon, \theta) = f_{in}$ at the inner contact, and $f(r = r_{out} + \varepsilon, \theta) = 0$ at the outer contact, where ε is infinitesimal.

S15. Temperature dependence of the outer contact resistance

The experiments described in Fig. 3b of the main text shows that as the temperature increases, a small step gradually builds up near the outer contact. We recall that in all the curves in that figure (corresponding to measurement temperatures from $T = 6\ K$ to $140\ K$) we subtracted the **same** contact step functions $R_c^{in}(r)$ and $R_c^{out}(r)$, those obtained from fitting the resistance profile at $T = 6\ K$ (Fig. 2c). This means that the contact steps that we see in Fig. 3b reflect the **difference** between the contact resistance at finite temperatures and that at $T = 6\ K$. The fact that we observe a finite outer contact step at high T therefore suggests that the outer contact resistance is larger at higher T.

In our Boltzmann numerical calculations (Fig. 3c) we observed a similar effect, but even stronger. There upon decreasing of l_{ee} (which corresponds to increasing T in the experiment) we see the buildup of a resistance step at the outer contact. We note that we use a similar procedure to the one used for the experimental curves - subtracting from all the Boltzmann curves the same contact resistance steps, the one obtained in the calculation with $l_{ee} = \infty$. The buildup of contact resistance step with decreasing l_{ee} in Fig. 3c therefore implies that the outer contact resistance increases with decreasing l_{ee}.

The Boltzmann calculation allows us to identify that this phenomenon originates from the transition between highly non-local ballistic flow at $l_{ee} = \infty$ and a locally equilibrated hydrodynamic flow at small l_{ee}. In a ballistic flow, the angular distribution of carriers in graphene, just outside the inner contact, has half of the angles populated by hot carriers emitted from the inner contact. Going toward the outer contact, the hot electrons get collimated to a smaller angular spread (the simple analogy would be the angle distribution of light rays reaching from the sun to an observer. As the observer gets further away from the sun, the distribution of light rays (/hot electrons) becomes more collimated). At a radius r the hot electrons are collimated to an angular spread of $\Delta\theta = 2\,\mathrm{asin}\left(\frac{r_{in}}{r}\right)$. As we have shown in the paper, the corresponding r dependence of the resistance is $R(r) = R_{sh}^{in}\frac{1}{\pi}\mathrm{asin}\left(\frac{r_{in}}{r}\right)$. For $r = r_{out} \gg r_{in}$ the collimated beam is very narrow, $\Delta\theta \approx 2\frac{r_{in}}{r_{out}}$. The outer contact resistance can be readily obtained from the value of the resistance function at r_{out}, since at the outer contact itself it equals zero. Namely, the theoretically predicted outer contact resistance in the ballistic regime is:

(ballistic) $$R_{contact}^{out} = R_{sh}^{in}\frac{1}{\pi}\mathrm{asin}\left(\frac{r_{in}}{r_{out}}\right) \approx R_{sh}^{in}\frac{1}{\pi}\frac{r_{in}}{r_{out}} \qquad \text{(S12.1)}$$

Indeed, this is the value that we obtain in the Boltzmann calculations in the ballistic regime ($l_{ee} = \infty$).

When we examine the Boltzmann calculations deep in the hydrodynamic case ($l_{ee} \ll r_{in}, r_{out}, r_{out} - r_{in}$) we see that we obtain a different outer contact resistance. In fact, in this case we observe that this resistance roughly equals the resistance one would obtain in the diffusive regime, namely, half the Sharvin resistance corresponding to r_{out}, $R_{sh}^{out} = \frac{\pi h}{4e^2} \frac{1}{k_F(2\pi r_{out})}$. Consequently,

(hydrodynamic) $$R_{contact}^{out} = \frac{1}{2} R_{sh}^{out} = R_{sh}^{in} \frac{1}{2} \frac{r_{in}}{r_{out}} \quad \text{(S12.2)}$$

At the same time, in the hydrodynamic regime, the angular distribution of the electrons near the outer contact is $\sim \cos(\theta)$. Comparing equations (12.1) and (12.2) we see that $R_{contact}^{out}$ in the hydrodynamic regime is larger by a factor $\pi/2$ than that in the ballistic regime (we ignore here higher orders in l_{ee}). This corresponds to the increase of outer contact resistance with decreasing l_{ee} seen in Fig. 3c. This factor reflects the fact that the current density carried by a highly collimated angular distribution is larger by a factor of $\pi/2$ than the current density carried by a $\cos(\theta)$ distribution.

S16. The dependence of the number of conduction modes on radius in a Corbino device.

As explained first by Landauer [14], the ultimate conductance of an electronic device is given by the number of its conduction modes times e^2/h (e is the electronic charge and h is plank's constant). The number of these modes is given by the ratio of the width of the device perpendicular to the current flow direction, W, divided by the Fermi wavelength, $\lambda_F = 2\pi/k_F$. In a standard Hall bar, the width of the device remains constant along the electronic flow direction, and thus the number of conduction modes remain fixed. In contrast, in a Corbino geometry, the effective device width perpendicular to the electronic flow direction increases with increasing radius. Consequently, the number of available quantum modes varies as $2\pi r/\lambda_F$, and thus it increases linearly with r. At the outer contact of a Corbino disk the number of modes is maximal. With decreasing radius it decreases because modes are being gradually terminated and the electrons that populate then get back-scatterd[15]. A simple way to understand this is to consider the angular momentum of each mode: defining the azimuthal and radial momenta of an electron by p_θ and p_r, the angular momentum from is given by $j = r \cdot p_\theta$. Due to the azimuthal symmetry of the Corbino, angular momentum is a conserved quantity, and thus it is a good quantum number. Angular momentum conservation further implies that when the electron propagates to a smaller r, its p_θ must increase as $1/r$. But since the linear momentum of the electron, $p = \sqrt{p_r^2 + p_\theta^2}$, is also a conserved quantity, the increase of p_θ necessarily leads to a corresponding decrease in p_r. For each mode there is a certain radius at which p_r becomes zero. This is the classical turning point of this mode, where the trajectory flips its radial flow from inwards to outwards. Based on these considerations, if we now plot [15] the number of modes existing at a given r we see again that it is linearly increasing with r.

S17. The physical significance of the resistance function $R(r)$.

In the main text we construct from the measured local potential, $\phi(r)$, and the measured total (2-probe) current, I, a resistance function, $R(r) = \phi(r)/I$. Below we explain its physical significance in the different transport regimes.

A key property of our devices that justifies defining a resistance function, which depends only on the radius, is their azimuthal symmetry. This symmetry is built into the lithographic structure of our Corbino devices. Furthermore, we observe this symmetry directly in the imaged two-dimensional potential maps (e.g. Fig. 2a), where we see that the azimuthal symmetry holds to an excellent degree (see quantitative analysis in Supp. Info. section S3). This symmetry suggests that the problem could be projected onto a one-dimensional problem, with the radius r being the only relevant coordinate. The geometry is taken into account in this projection since the function $R(r)$ describes the accumulated resistance of two-dimensional rings up to a radius r.

A transport regime which is of primary interest in this paper is the hydrodynamic regime. Well within the hydrodynamic regime, the transport equations are local. Thus, in this regime the function $R(r)$ has a clear physical meaning. Specifically, $R(r_1) - R(r_2)$ represents the resistance contributed from the ring between radii r_1 and r_2.

In the ballistic regime the transport becomes non-local, and thus the meaning of local contributions to resistance becomes more poorly defined. Yet, even in the ballistic regime the function $R(r)$ has a physically significant meaning. This function describes how the resistance is divided between the bulk and the contacts. Specifically, if we place the outer contact at a radius r, then $R(r)$- $R(r_{in})$ describes what part of the Landauer-Sharvin resistance will drop in the bulk of the Corbino disk. Theoretically, this is precisely the resistance component that can be gained if the flow becomes hydrodynamic.

S18. Accuracy of the measured $R(r)$ due to the sensitivity of the Nanotube SET

The voltage sensitivity is defined as[3]

$$n_v = \sqrt{< I_0^2 >} \left(\frac{\partial I_{SET}}{\partial V_{SET}}\right)^{-1} \frac{C_{SET}}{C_{Sample}} \frac{A}{\sqrt{\Delta f}}$$

Where Δf is the sampling bandwidth, A is the correlation factor to account for the sampling window function, $\frac{C_{SET}}{C_{Sample}}$ is the capacitance ratio between SET and sample, $\frac{\partial I_{SET}}{\partial V_{SET}}$ is the transconductance of the SET with its local gate and $\sqrt{< I_o^2 >}$ is the current variance measured by SET. The distance between the local gate and the SET distance in this experiment $220\ nm$ and our scanning height above the sample is $\sim 800\ nm$, implying that $\frac{C_{SET}}{C_{Sample}} \sim 4$. The base noise of the SET used in this experiment at $f \sim 1\ kHz$ is $\sim 2.5\ \mu V/\sqrt{Hz}$. After scaling it with the capacitance ratios above we get that the noise level in measurements of the sample potential is $\sim 10\ \mu V/\sqrt{Hz}$. The measurement time per pixel in a typical 2D image (e.g. figure 2a) was 0.4sec, giving noise level of $\sim 20\ \mu V/pixel$. We obtain the $R(r)$ profiles by radial averaging over such 2D images. A typical 2D scan has 150 x 150 points and is averaged to a grid in r with about $100nm$ between pixels. The noise level in ϕ improves due to the radial averaging as the square root of the number of points included in the averaging, $\sqrt{n_p} \sim \sqrt{20 \cdot \frac{r}{1\mu m}}$. For our measurement parameters this leads to a noise of $3\ \mu V$ for a pixel in $\phi(r)$ trace at $r = 2\ \mu m$ and $1.5\ \mu V$ at $r = 9\ \mu m$. For a typical total current in our measurement at ($\sim 100\ \mu A$ at $T = 6\ K$), the noise level in each pixel of the $R(r)$ trace is therefore $\sim 2 \cdot 10^{-2} \Omega$. In some of the curves (e.g. Fig. 3a) we averaged 20 images measured sequentially, to obtain another factor of 4 improvement.

References:

1. Wang, L. *et al.* One-Dimensional Electrical Contact to a Two-Dimensional Material. *Science (1979)* **342**, 614–617 (2013).

2. Kim, Y., Herlinger, P., Taniguchi, T., Watanabe, K. & Smet, J. H. Reliable Postprocessing Improvement of van der Waals Heterostructures. *ACS Nano* **13**, 14182–14190 (2019).

3. Ella, L. *et al.* Simultaneous voltage and current density imaging of flowing electrons in two dimensions. *Nature Nanotechnology* **14**, 480–487 (2019).

4. Ben Shalom, M. *et al.* Quantum oscillations of the critical current and high-field superconducting proximity in ballistic graphene. *Nature Physics* **12**, 318–322 (2016).

5. Efetov, D. K. & Kim, P. Controlling Electron-Phonon Interactions in Graphene at Ultrahigh Carrier Densities. *Physical Review Letters* **105**, 256805 (2010).

6. de Jong, M. J. M. & Molenkamp, L. W. Hydrodynamic electron flow in high-mobility wires. *Physical Review B* **51**, 389–402 (1995).

7. Ditlefsen, E. & Lothe, J. Theory of size effects in electrical conductivity. *Philosophical Magazine* **14**, 759–773 (1966).

8. Moll, P. J. W., Kushwaha, P., Nandi, N., Schmidt, B. & Mackenzie, A. P. Evidence for hydrodynamic electron flow in PdCoO 2. *Science (1979)* **351**, 1061–1064 (2016).

9. Scaffidi, T., Nandi, N., Schmidt, B., Mackenzie, A. P. & Moore, J. E. Hydrodynamic Electron Flow and Hall Viscosity. *Physical Review Letters* **118**, 226601 (2017).

10. Callaway, J. Model for lattice thermal conductivity at low temperatures. *Physical Review* **113**, 1046–1051 (1959).

11. Gennaro, S. de & Rettori, A. The low-temperature electrical resistivity of potassium: size effects and the role of normal electron-electron scattering. *Journal of Physics F: Metal Physics* **14**, L237–L242 (1984).

12. Gennaro, S. de & Rettori, A. On the electron-electron contribution to the low-temperature electrical resistivity of thin wires. *Journal of Physics F: Metal Physics* **15**, 2177–2188 (1985).

13. Courant, R. & Hilbert, D. Methods of Mathematical Physics. *Methods of Mathematical Physics* **2**, 1–830 (2008).

14. Landauer, R. Spatial Variation of Currents and Fields Due to Localized Scatterers in Metallic Conduction. *IBM Journal of Research and Development* **1**, 223–231 (1957).

15. Stern, A. *et al.* Spread and erase - How electron hydrodynamics can eliminate the Landauer-Sharvin resistance. *arXiv: 2110.15369* (2021).